Article

# Compositional, Optical and Electrical Characteristics of $SiO_x$ Thin Films Deposited by Reactive Pulsed DC Magnetron Sputtering

**Joaquim O. Carneiro [1,*], Filipe Machado [1], Luis Rebouta [1], Mikhail I. Vasilevskiy [2,3], Senen Lanceros-Méndez [2,4], Vasco Teixeira [1], Manuel F. Costa [2,*] and Anura P. Samantilleke [1]**

1. Centre of Physics, Department of Physics, University of Minho, Azurém Campus, 4800-058 Guimarães, Portugal
2. Centre of Physics, Department of Physics, University of Minho, Gualtar Campus, 4710-057 Braga, Portugal
3. International Iberian Nanotechnology Laboratory, Avenida Mestre José Veiga, 4715-330 Braga, Portugal
4. Basque Center for Materials, Applications and Nanostructures, UPV/EHU Science Park, 48940 Leioa, Spain

* Correspondence: carneiro@fisica.uminho.pt (J.O.C.); mfcosta@fisica.uminho.pt (M.F.C.); Tel.: +351-253-510-400 (J.O.C.); +351-253-604-070 (M.F.C.)

Received: 20 June 2019; Accepted: 22 July 2019; Published: 25 July 2019

**Abstract:** The influence of $O_2$ flow rate on the compositional, optical and electrical characteristics of silicon oxide ($SiO_x$) thin films ($x < 2$) were studied in this work. The $SiO_x$ thin films were obtained by pulsed direct current (DC) magnetron sputtering (PMS) onto n-type Si wafers (and also on glass substrates) at a vacuum of $3 \times 10^{-3}$ Pa. Rutherford backscattering spectrometry (RBS) was used to check the compositional elements of deposited films and its oxidized states were analysed via Fourier-transform infrared (FTIR) spectroscopy. The optical properties of as-deposited $SiO_x$ thin films were investigated from transmittance measurements at room temperature in the wavelength range of 250–800 nm. The obtained data reveal that the Urbach energy (a measure of the band tail extension, $E_u$) decreased from about 523 to 172 meV as the rate of oxygen gas flow increased. On the contrary, the optical energy band-gap ($E_g$) increased from 3.9 to 4.2 eV. Conduction and valance band positions (relative to the normal hydrogen electrode) were also evaluated. The observed behavior is probably associated with the degree of disorder and defects presented in the as-deposited $SiO_x$ thin films, probably due to the presence of newly inserted oxidized $O_nSiH_y$ species resulting from some contamination with water vapor desorbed from the walls of the deposition vacuum chamber. After deposition of a gold top electrode, the electrical characteristics of the fabricated Au/$SiO_x$/*n*-Si system (i.e., a metal/insulator/semiconductor structure—MIS) were studied via characteristic *I-V* curves and their dependence upon the $O_2$ flow rate are reported. It was observed that the Au/$SiO_x$/*n*-Si structure behaves like a Schottky-diode exhibiting a very good diode rectifying performance with a rectification ratio of at least 300 and up to $10^4$, which refers to the samples produced with the lower and higher $O_2$ flow rates, respectively. It was also found that the $O_2$ flow rate influences the rectifying performance of the $SiO_x$/*n*-structures since both the diode ideality factor, $n$, and the diode series-resistance, $R_S$ decreases with the increase of $O_2$ content, possibly reflecting a closer approximation to a full stoichiometric condition.

**Keywords:** pulsed DC magnetron sputtering; silicon oxide; Urbach tail; *I-V* characteristics

## 1. Introduction

In recent years, silicon oxide ($SiO_x$) based coatings (a combination of stoichiometric oxide ($SiO_2$) with a non-stoichiometric sub-oxide ($SiO_x$, $x < 2$) [1]) have been studied due to their technological importance in numerous applications, including microelectronics [2], communication [3],

pharmaceutical, food and packaging industries [4,5]. The use of silicon oxide coatings as a dielectric insulator of electronic switches and sensing devices such as thin-film transistors (TFTs), metal-insulator-semiconductor (MIS) switching devices, optical coatings and optoelectronic applications or even in processes associated with the fabrication of micro-electromechanical-systems (MEMS), serving for example, as etch masks in bulk micromachining or as sacrificial layer in surface micromachining processes [6–9] is particularly noteworthy due to its properties, as $SiO_x$ compounds are known to have good abrasion resistance, electrical insulation, high thermal stability and also being insoluble in the majority of acids. There are several techniques to produce silicon dioxide films among which one of the most common is the thermal oxidation method [10–12]. However, this thermal technique presents some drawbacks such as high temperature, which is usually higher than 900 °C, highly clean surface required for diffusion process, low deposition rate (it may need hours for moderately thick coatings) and also the requirement of silicon wafer as the only substrate. Fortunately, there are other deposition techniques that can be used to produce $SiO_x$ coatings such as direct current (DC) reactive magnetron sputtering (MS) [13,14], electron beam evaporation with ion assistance [15–17], low-pressure chemical vapour deposition (LPCVD) [18], hot filament chemical vapour deposition (HFCVD) [19] and plasma-enhanced chemical vapour deposition (PECVD) [20]. However, since LPCVD, HFCVD, and PECVD deposition techniques require high temperature, these techniques are not suitable for materials with low melting point.

Sputtering techniques are clearly suitable to deposit silicon dioxide thin films. The utilization of MS technique to deposit metal oxides coatings can lead to the generation of arcs and plasma instability. On the other hand, reactive pulsed DC magnetron sputtering (PMS), besides being able to reduce or even eliminate arcs, this technique can also be used to deposit at low-temperature metal oxide-based coatings with high-quality characteristics [21,22] and also, when compared with radio frequency (RF) sputtering, PMS technique is a relatively more competitive and attractive deposition method because it implies low-cost in industrial settings for mass production.

Although in recent years most of the research work performed in the field of physical deposition of metal oxide-based coatings has been devoted to RF sputtering technique, it appears that much fewer studies have been reported on the development and characterization of silicon oxide-based thin films by produced by PMS technique. In this sense, the main motivation and contribution of this work is to complement the investigation, study and estimation of some other optical and electrical properties of $SiO_x$ thin films, which have not been exposed in previous literature studies, which mainly refers to Urbach's parameters [23] and Schottky-diode [24–26] rectifying characteristics of $SiO_x$/$n$-Si structures (after the deposition of a Au top electrode onto its surface) produced by PMS deposition method. In particular, our goal is to discuss the correlation between these parameters (band tail width, $E_u$, energy band-gap, $E_g$, diode ideality factor, $n$, and diode series-resistance, $R_s$) with the different amounts of $O_2$ gas flow utilized in the fabrication of $SiO_x$/$n$-Si structures.

## 2. Experimental Details

### 2.1. Deposition of $SiO_x$ Thin Films by Pulsed DC Magnetron Sputtering

Traditionally, DC reactive magnetron sputtering can be separated into three different modes, namely (I) the metallic, (II) the transition and (III) the compound (or reactive) mode. These operation 'regimes' are a function of the amount of used reactive gas during deposition [27]. By using reactive pulsed DC magnetron sputtering technique, it is possible to minimize or even suppress the generation of arcing events in the target surface, which result from its poisoning during the compound mode. Specific details of PMS deposition method have already been described in our previous work [28]. Briefly, in PMS deposition method there are two different parameters that are experimentally adjusted in the voltage waveform, which refer to the pulsed frequency, $f$ and the reverse time, $t_r$.

These two parameters are related to the so-called reverse phase, $\tau_r$ through the following relation: $\tau_r$ (%) = ($t_r \times f$) × 100, where $f$ is the frequency of the applied pulse. It should be noted that most

commercial available pulsed sources limit the reverse voltage (i.e., the target positive voltage, $V_r$) to a value that typically corresponds to 10% of the negative applied voltage, $V_0$. This practice is sufficient to effectively dissipate the charged regions and thus prevent arcing events. In this work, the $SiO_x$ thin films were deposited on n-type 380-µm-thick (100) Si wafers by using a homemade PMS system).

It is important to mention that, in order to perform transmittance spectroscopy over the $SiO_x$ thin films, glass substrates were also used in the same deposition conditions. The target used in this work was a Si disk (purity 99.99%) with a diameter of 70 mm and the used target-to-substrate distance ($z$) was $z$ = 70, 80 and 90 mm in which the shortest distance ($z$ = 70 mm), was utilized to deposit samples with the highest $O_2$ gas flow and the largest one ($z$ = 90 mm) was selected to produce samples with the lowest $O_2$ gas flow. After evacuating the chamber to a base pressure lower than $3 \times 10^{-3}$ Pa, the target surface was firstly etched (during 15 min) by $Ar^+$ ion bombardment while the shutter was kept closed to prevent contamination of the substrate with any undesirable material. After the etching step, $O_2$ gas was injected into the chamber through a 6 mm gas ring opening located at about 100 mm from the magnetron-sputtering source. The sputtering of target surface proceeded at a working pressure of about $1.4 \times 10^{-1}$ Pa and under a constant current of 0.35 A (current density of 9.1 mA/cm$^2$). A mass-flow controller (Bronkhorst, Suffolk, UK) was used to measure the Ar and $O_2$ flows. For all produced samples, the argon flow was kept at a constant value of 8 sccm while the flow of $O_2$ gas was varied in order to obtain $SiO_x$ coatings grown under three different $O_2$ gas flows, corresponding to samples that from now will be identified (ID) as @1.4, @1.6 and @2.0. The deposition time for all the produced $SiO_x$ coatings was 60 min. The main deposition parameters are shown in Table 1.

**Table 1.** Parameters used in pulsed direct current (DC) magnetron sputtering of $SiO_x$ thin films.

| Sample ID | Current (A) | Voltage (V) | Reverse Time (µs) | Frequency (kHz) | Gas Flow (sccm) | | Reverse Phase (%) |
|---|---|---|---|---|---|---|---|
| | | | | | Ar | $O_2$ | |
| @1.4 | | 385 | | | | 1.4 | |
| @1.6 | 0.35 | 217 | 5.0 | 60.0 | 8.0 | 1.6 | 30.0 |
| @2.0 | | 210 | | | | 2.0 | |

### 2.2. Film Characterization

Fourier transform infrared (FTIR) spectroscopy was used in order to obtain structural information for the as-deposited $SiO_x$ thin films. FTIR spectra were acquired on an IR Affinity-1S spectrophotometer (Shimadzu, Kyoto, Japan) in a frequency range from 380 to 4000 cm$^{-1}$. Rutherford backscattering spectrometry (RBS) measurements were carried out at the CTN/IST Van de Graaff accelerator with detectors placed at 165° to the beam direction using a 2 meV $^4He^+$ beam. Normal incidence was used in the experiments and the obtained data were analyzed with the IBA Data Furnace [29].

Optical studies were performed to determine the absorption coefficient $\alpha(\lambda)$, the band tail width quantified by the so-called Urbach energy ($E_u$) and the optical gap ($E_g$). These optical parameters were obtained by using transmission $T(\lambda)$ measurements performed with a UV-3101PC UV–Vis-NIR spectrophotometer (Shimadzu, Kyoto, Japan). The transmittance signal was collected from 250 to 800 nm with a resolution of 1.0 nm. The film's surface morphology was obtained by scanning electron microscopy (SEM) (NanoSEM—FEI Nova 200 (FEG/SEM) equipment, FEI, Hillsboro, OR, USA).

In order to investigate the electrical characteristics of the $SiO_x$/$n$-Si system, current-voltage ($I$-$V$) characteristic curves were measured by means of a Keithley 487 picoammeter (Keithley, Cleveland, OR, USA)/voltage source under a voltage range from −1.0 to 1.0 V in steps of 0.1 V. It is important to note that before acquiring the $I$-$V$ characteristic curves, gold and aluminum contacts were firstly deposited as top and back electrodes, respectively on the $SiO_x$/$n$-Si heterostructure (see Figure 1), which resembles a Schottky diode structure [24].

The Au top electrode was deposited with a circular shadow mask (1.0 mm diameter) on the $SiO_x$ surface by resistive thermal evaporation of 34 mg of gold (from an Au wire with 0.5 mm diameter)

previously placed inside a tungsten boat. Complete evaporation of the Au wire was attained by applying a current of 200 A under a voltage of 1.0 V for 1 min, which ensured the deposition of an Au layer of about 150 nm (estimated from SEM analysis).

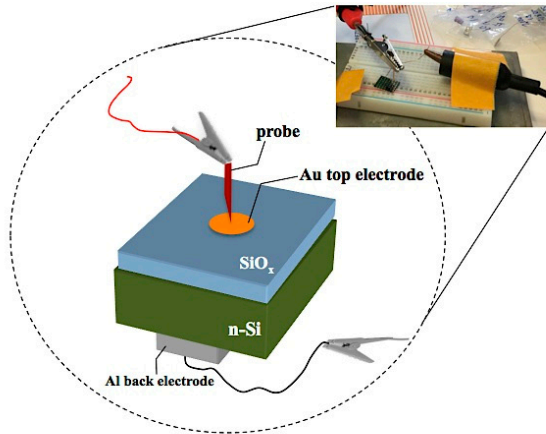


**Figure 1.** Experimental set-up for measuring of *I-V* characteristics and schematic representation of Au/$SiO_x$/*n*-Si structure.

## 3. Results and Discussion

### 3.1. Target Voltage Control Method and Hysteresis Effect

The most used and reliable technique in controlling reactive sputtering processes is the so-called target voltage control method, a simple and low-cost procedure. Figure 2 shows the target voltage as a function of the oxygen gas flow rate [$O_2$/($O_2$ + Ar)]%, which presents a hysteresis loop.

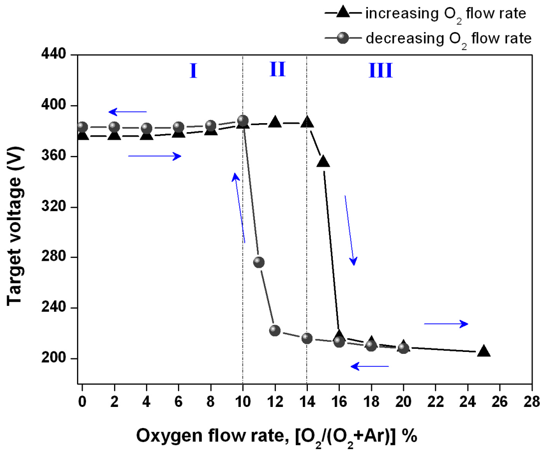


**Figure 2.** Hysteresis behaviors of target (cathode) voltage as a function of reactive $O_2$ gas flow rate.

As can be observed, for low values of $O_2$ gas flow rate (region I), the sputtered "metal" gathers almost all the available reactive gas because target voltage has practically no changes and the deposited film is under the so-called "metallic" mode ("metal"-rich). However, as the reactive gas flow rate continues to increase until it reaches a certain critical value, one can observe a sharp decrease in the target voltage, which corresponds to the point where the target becomes poisoned (the compound mode, i.e., region III). Under this condition, the sputtered "metal" does not fully gather the flow rate of the reactive gas entering into the deposition chamber, thus the deposited films should be reactive gas-rich. It is noteworthy that the variations of the target voltage depend on changes in target surface composition as it determines the amount of secondary electrons emitted by ion bombardment on the

target surface [30]. Once the target is poisoned, its voltage does not change following the same path to return to the "metallic mode", as the level of $O_2$ reactive gas remains still high until the compound layer, which was previously formed on the target surface, is entirely removed uncovering original target material.

Therefore, according to the deposition parameters presented in Table 1, the sample identified as @1.4, having been deposited at the lower limit of the compound mode, is expected to lead to a silicon-rich and oxygen-deficient coatings. The samples coded as @1.6 and @2.0 are likely to be $O_2$ richer and hence, possibly closer to the stoichiometric condition.

It is important to refer that, for the same deposition times, the use of different $O_2$ gas flow directly influences the thickness ($d$) of the $SiO_x$ films, unless the target-to-substrate distance is suitably varied. In this work, the thickness $d \approx 500$ nm (determined from SEM) of the as-deposited $SiO_x$ films is basically the same and this was achieved through an empirical adjustment (trial and error) of the target-to-substrate distance.

The thickness of a coating produced by magnetron sputtering is related to its growth rate, which in turn is influenced by the sputter yield ($Y$) and also on the mean free path of target atoms. Considering elastic binary collisions, only kinetic energy is exchanged, while the potential energy is conserved as it mainly resides within the electronic structure of the colliding atoms, ions, molecules, etc.) [31]. Taking elastic binary and central collisions between atoms, and assuming that one of the atoms is initially stationary, the well-known result is

$$\chi = \left(\frac{E_2}{E_1}\right) = \frac{4m_1m_2}{(m_1 + m_2)^2} \tag{1}$$

where $m_1$ and $m_2$ refer to the mass of incident and target atoms, respectively, whereas $E_1$ is the initial kinetic energy of the incident atom and $E_2$ is the energy of target atom after collision. The quantity $4m_1m_2/(m_1 + m_2)^2$ (or $E_2/E_1$) is known as the energy transfer function, $\chi$.

For example, if $m_1 = m_2$ then $\chi = 1$, that is, after collision the initial moving atom is stopped, and its kinetic energy is totally transferred to the second atom, which moves away. In this work, the incident "particles" are argon atoms (Ar ≈ 39.9 amu) and taking the target composed by silicon atoms (Si ≈ 28.08 amu), its energy transfer function is $\chi_{\mathrm{Si}} = 0.969$, which is quite close to unity and thus, resulting in a safe arrival of Si atoms to the substrate. On the other hand, if the target surface is poisoned with the oxygen reactive gas (i.e., the silicon atoms are shielded by O atoms), the energy transfer function for oxygen (O ≈ 15.99 amu) is $\chi_{\mathrm{O}} = 0.817$. This means that, during collisions, argon atoms transfer much less energy to the oxygen ones. In this sense, any eventual collision occurring between Ar and O during the path of the O atoms from the target to the substrate will result in moving away the O atoms because in general, they may not have gained enough energy to overcome the target-to-substrate distance. This condition leads to a decrease in the amount of oxygen in the substrate, which has direct repercussions on the thickness (decrease) of the deposited coating. Meanwhile, the sputter yield is the number of atoms (or molecules) ejected from a target surface per incident atom (ion) and is a measure of the efficiency of sputtering [31]. The sputter yield is proportional to the energy transfer function and varies inversely with the surface binding energy ($E_{\mathrm{b}}$) of a particular atom [32]

$$Y \propto \chi \frac{E_2}{E_1} \tag{2}$$

It is interesting to evaluate the order of magnitude for the ratio between the sputter yields for silicon and oxygen. The binding energies for silicon and oxygen are 4.73 and 6.79 eV, respectively [33]. The application of Equation (2) predicts that the oxygen sputter yield is almost half that of the silicon, that is, $Y_{\mathrm{O}}/Y_{\mathrm{Si}} = 0.587$. This is the reason why that, in this work, the target-to-substrate distance was slightly varied, since the shortening of the target-to-substrate distance represents a strategy to counteract the effect of a lower sputtering yield. Since all the produced samples were essentially

deposited under the same working pressure ($1.4 \times 10^{-1}$ Pa), then the mean free path for each sputtered atom is basically the same. Therefore, a smaller target-to-substrate distance decreases the probability of sputtered atoms to be scattered by incident argon ions, and thereby causing an increase of the growth rate and, consequently, in the achieved thickness.

In this sense, one can expect that for elements having lower sputter yields and sputtered with lower target-to-substrate distances would form coatings with thicknesses similar to those formed by elements that have been sputtered with higher sputter yields, but at longer target-to-substrate distances.

## 3.2. Film Characteristics

It is well known that infrared spectroscopy (IR) is a powerful tool to monitor the change of oxidized states due to its high sensitivity to molecular structures. The IR absorption spectra of the $SiO_x$ films deposited with three different flow rates of $O_2$ reactive gas were measured by using FTIR covering a wavenumber range from 380 to 4000 $cm^{-1}$. In order to compare the oxidized states of the as-deposited $SiO_x$ thin films with the fully stoichiometric silicon dioxide (or silica/$SiO_2$), a IR absorption spectrum was also performed on pure silica, in its powder form (0.5 µm particle size), previously purchased from Sigma-Aldrich (Saint Louis, MO, USA). Figure 3 shows the IR absorption spectra of $SiO_x$ films (and also of silica for comparison) acquired in the low-frequency region (380 to 1400 $cm^{-1}$). Table 2 presents the peaks' position of the Si–O bonds.

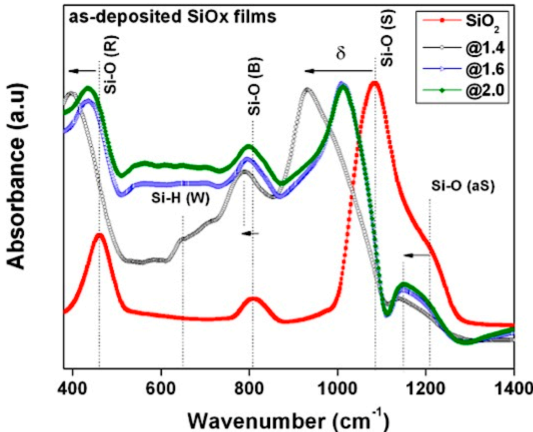


**Figure 3.** Fourier-transform infrared (FTIR) spectra for the as-deposited $SiO_x$ films and also for stoichiometric $SiO_2$ (silica powder). δ is the deviation from stoichiometry.

**Table 2.** FTIR vibration modes for as-deposited $SiO_x$ films [34–36].

| Vibration Mode | Peak Position ($cm^{-1}$) | | | |
|---|---|---|---|---|
| | Sample ID | | | |
| | @1.4 | @1.6 | @2.0 | $SiO_2$ |
| Si–O rocking | 397 | 438 | 440 | 461 |
| Si–O bending | 789 | 797 | 799 | 810 |
| Si–O stretching (on phase) | 932 | 1010 | 1013 | 1082 |
| Si–O stretching out of phase | 1140 | 1148 | 1150 | 1203 |
| Si–H wagging | 648 | – | – | – |

Three main absorption characteristic peaks of Si–O–Si group, namely 461 $cm^{-1}$ for the Si–O vibration rocking mode, 810 $cm^{-1}$ for the Si–O bending mode and 1082 $cm^{-1}$ for the Si–O stretching mode can be identified by analyzing the IR spectra [34,35]. In fact, the main information extracted from the examination of IR spectra refers to a downward shift toward a lower wavenumber that occurs for the generality of the peaks' position of Si–O bonds as the $O_2$ gas flow is decreased. For example, the strongest absorption peak is ascribed to the Si–O stretching vibration mode where its position

shifted from 1082 $cm^{-1}$ (stoichiometric $SiO_2$) towards a lower frequency of 932 $cm^{-1}$, which corresponds to $SiO_x$ thin films produced under the lower $O_2$ flow rate. These results indicate that the decrease of $O_2$ content promotes a change in the oxidation state of the as-deposited films, from an oxygen excess to a more silicon-rich thin films (non-stoichiometric) where the Si–O bonds are progressively replaced by Si–Si bonds [37]. Additionally, it is also observed that the shoulder (1203 $cm^{-1}$) existing in stoichiometric $SiO_2$, assigned to the out of phase stretching (or asymmetric stretching mode) mode of Si–O–Si [34,35], changes to a prominent peak, which slightly moves toward a lower frequency as $O_2$ gas flow rate is decreased. Moreover, it was also calculated the ratio of absorption intensities between the peaks associated with the in-phase and out of phase stretching modes. The ratio for stoichiometric $SiO_2$ is 0.38, whereas for the as-deposited $SiO_x$ films, it decreases as the $O_2$ gas flow also decrease, namely from 0.23, 0.19 to 0.17, corresponding to the samples @2.0, @1.6, and @1.4, respectively. These results reveal that as the $O_2$ gas flow is reduced, the obtained ratios are further away from that of the stoichiometric $SiO_2$. According to the results shown in Table 2 and also in Figure 4, it is suggested that the main physical reason for the shift of the characteristic dipole-active vibration modes towards lower frequencies (Si-rich films) with the increase of the deviation from stoichiometry, $\delta$ is related to the increase in the average bond length, so it becomes less stiff.

In addition, Figure 3 also shows a weak absorption peak at 648 $cm^{-1}$ detected for the $SiO_x$ film deposited under the lower oxygen content (i.e., the @1.4 sample), which has been identified as being associated with Si–H wagging bonds [38]. The surprising appearance of hydrogen atoms has raised our interest in extending the FTIR spectra to the region of high frequencies. Figure 4a presents the IR absorption spectra for the $SiO_x$ films deposited under different $O_2$ gas flows in the range from 1400 to 4000 $cm^{-1}$. The FTIR spectra show four distinct Si–H stretching vibrations at 1980, 2025, 2162, and 2376 $cm^{-1}$, which can be ascribed to the –OSi–H, –OSi–$H_2$, –OSi–$H_3$, and –$O_2$Si–H partially oxidized structures [39], respectively. The geometries of these structures [39] are shown in Figure 4b and the corresponding vibration modes of those different oxidized states are presented in Table 3.

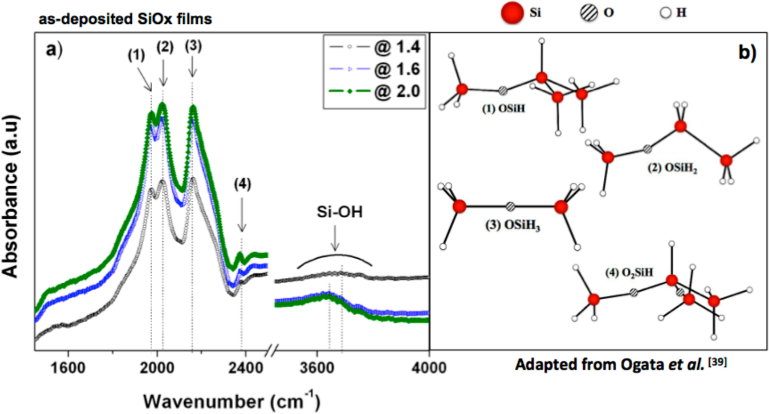


**Figure 4.** Spectra acquired in high-frequency range for the as-deposited $SiO_x$ films (**a**) and structural geometries of the different oxidized states (**b**).

**Table 3.** Frequencies and type of vibrations modes in high-frequency range for the as-deposited thin films [39].

| Group | Cluster | Peak Number | Vibration Type | Wavenumber ($cm^{-1}$) |
|---|---|---|---|---|
| $SiH_3$ | $OSiH_3$ | (3) | s-stretching | 2162 |
| $SiH_2$ | $OSiH_2$ | (2) | a-stretching | 2025 |
| SiH | OSiH | (1) | stretching | 1980 |
| | $O_2SiH$ | (4) | stretching | 2376 |

The weak but broadband absorptions shown in Figure 4a around 3650 $cm^{-1}$ are due to the presence of $H_2O$ and are attributed to the O–H stretching vibrations. This suggests that during the high vacuum

phase of the deposition process, some amount of water vapor was desorbed from the walls of the vacuum chamber. Therefore, the "atmosphere" within the chamber was undesirably contaminated with hydrogen and additional oxygen atoms during the deposition process. Under this scenario, it has been pointed out that the presence of water promotes oxidation acceleration, once $H_2O$ is capable of attacking and breaking a Si–Si bond, thus producing extra SiH and SiOH species [40]. These newly inserted $SiH_x$ species are now quite likely to experience further oxidation to form $O_nSiH_x$ species (where $n$ = 1 to 3 and $x$ = 1 to 3) [39]. In this condition, the presence of $H_2O$ acts as an additional and contaminating source of hydrogen atoms. In this sense, it is suggested that hydrogen atoms are capable of competing with the reactive $O_2$ gas to form bonds with the silicon atoms that have been sputtered by $Ar^+$ ion bombardment. Thus, it will be quite improbable to obtain a stoichiometric $SiO_2$ film and instead, non-stoichiometric silicon oxide $SiO_x$ films should predominate in the presence of another type of partially oxidized species in the form of $O_nSiH_x$ species.

Figure 5 shows the RBS spectrum for the @1.4 sample, with a composition of 33.7 at %, 65.9 at % and 0.4 at % of Si, O, and residual Ar, respectively.

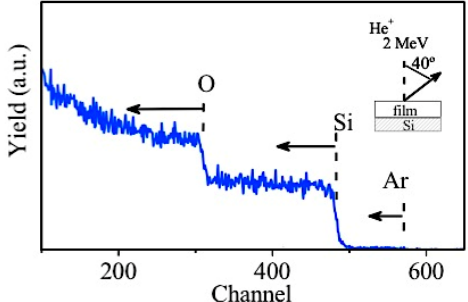


**Figure 5.** Rutherford backscattering spectrometry (RBS) spectrum of a $SiO_x$ layer (for sample @1.4). Arrows specify surface peaks of O, Si, and Ar.

Figure 6 shows the evolution of Si atomic concentration (at %) for the as-deposited $SiO_x$ films as a function of the different $O_2$ gas flows, which also includes the variation of the O/Si ratio.

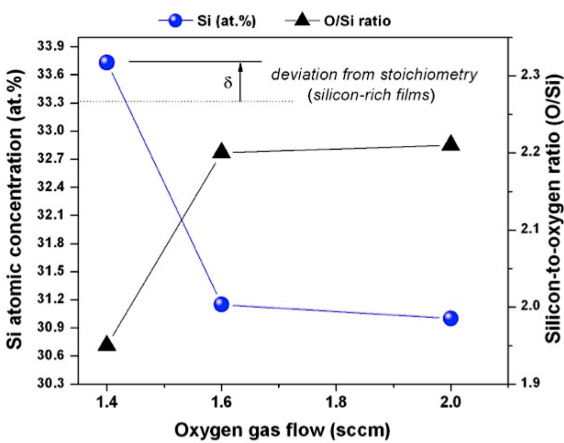


**Figure 6.** Si atomic concentration (at %) and O/Si ratio measured by RBS as a function of the $O_2$ gas flow.

According to Figure 6, it is possible to infer that the higher Si atomic concentration (low oxygen content) corresponds to sample deposited with 1.4 sccm of $O_2$ gas flow and it diminishes rapidly when the reactive $O_2$ gas flow is increased to 1.6 sccm. However, the Si atomic content practically does not change when the $O_2$ flow rate is increased again to 20%. On the other hand, it is also observed that the films deposited under 1.6 sccm and 2.0 sccm of $O_2$ gas flows have essentially the same O/Si ratio, denoting oxygen-rich $SiO_x$ films. For the films deposited with a reactive $O_2$ gas flow of 1.4 sccm, the O/Si ratio is 1.95, thus involving oxygen-deficient films and lower Si oxidation state. These results

are totally in agreement with the ones obtained by FTIR, since in the lower frequency-region of the FTIR spectra, the lower O/Si ratio also caused a shift in characteristic dipole-active vibration modes towards lower frequencies, as shown in Figure 3 and Table 2. Knowing the film's thickness, the optical absorption coefficient $\alpha(\lambda)$ was determined from the transmittance measurements by using the relation [41],

$$\alpha(\lambda) = \frac{1}{d}\ln\left[\frac{(1 - R)^2}{T(\lambda)}\right] \quad (3)$$

where $\lambda$ is the wavelength of the of incident photon, $T(\lambda)$ is the transmittance at a particular wavelength, $R$ is the reflectance ($R \leq 5\%$) and $d \approx 500$ nm is the thickness of the as-deposited $SiO_x$ films measured by SEM.

In non-crystalline $SiO_2$, although there is no long-range order, its electronic structure is similar to the electronic structure of α-quartz, the crystalline form of $SiO_2$. However, the absorption spectra, as in any disordered material, extend to energies well below the absorption threshold of the crystalline counterpart. Even though the so-called Tauc plot [42] may be used to determine a kind of band-gap energy by extrapolation, this parameter not always is quite meaningful because its value depends very much on the choice of the (limited) spectral range used for extrapolation. Experimentally, the sub-gap absorption in many disordered materials is known to obey the Urbach rule [23,43],

$$\alpha(\lambda) = \alpha_0 \exp\left[\sigma\frac{\hbar\omega - E_g}{k_B T}\right] \quad (4)$$

where $\alpha_0$ is a constant, $\hbar$ is the reduced Planck constant, $E_g$ is an effective band-gap energy, $\omega = 2\pi c/\lambda$ is the frequency of the incident photon, $k_B$ is the Boltzmann constant, $T$ is the temperature and $\sigma$ is a dimensionless material parameter often called the steepness parameter. Note that the temperature dependence implies the participation of phonons [44]. The steepness parameter ($\sigma$) is connected with the Urbach energy ($E_u$) through the relation [45],

$$E_u = \frac{k_B T}{\sigma} \quad (5)$$

This energy may be interpreted as the band tail width: It is weakly dependent on temperature and describes localized states that exist in the bandgap of disordered materials [43,46]. Both $E_g$ and $E_u$ are usually considered as fitting parameters in Equation (4) [47].

The dependence of the optical absorption coefficient, $\alpha(\lambda)$, of the produced $SiO_x$ thin films upon the incident photon wavelength is depicted in Figure 7.

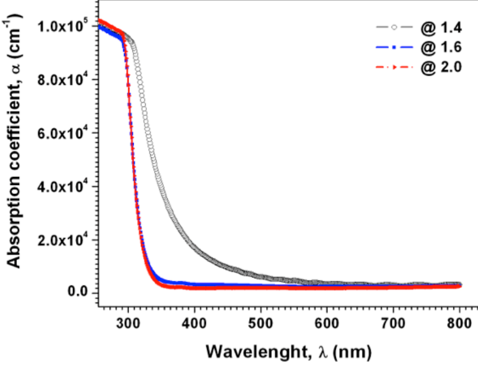


**Figure 7.** The variation of the optical absorption coefficient for different $SiO_x$ thin films.

The analysis of the figure shows that, for all samples, the value of the absorption coefficient decreases with the increase of the incident photon wavelength till to a certain value, from which it becomes almost invariant. It is also observed that the decrease of $\alpha(\lambda)$, is much more pronounced

for the samples produced with the $O_2$ gas flows of 1.6 and 2.0 sccm, whose spectra are essentially overlapped with each other. For these samples, the absorption edge is about 290 nm whereas for the sample identified as @1.4 (i.e., Si-rich sample) it is shifted to a higher wavelength (≈325 nm), thus suggesting a lower energy bandgap than for other two samples.

Figure 8 shows the plot of $\log\alpha$ versus photon energy ($\hbar\omega$) in the range of the Urbach tail.

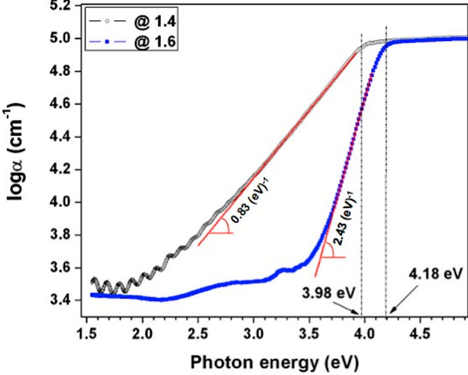


**Figure 8.** The variation of $\log\alpha$ with the incident photon energy ($\hbar\omega$), from which the Urbach energy for $SiO_x$ thin films was obtained.

The value of $E_u$ can be obtained from the reciprocal of the slope of the straight line of plotting $\log\alpha$ against the incident photon energy. On the other hand, $E_u$ can be possibly estimated as the position of the point where the exponential behavior of $\alpha$ (in normal scale, according to Equation (4)) changes to a slower (potential function) increase with $\hbar\omega$. This estimation is demonstrated in Figure 8 through representation with dashed vertical lines. Anyway, after fitting the Urbach absorption tails with Equation (4), the obtained values of the Urbach energy, the band-gap energy, the $\alpha_0$ constant and the steepness parameter ($\sigma$) are listed in Table 4.

**Table 4.** The values of the Urbach energy ($E_u$), direct forbidden bandgap energy ($E_g$), steepness parameter ($\sigma$) and the pre-exponential constant ($\alpha_0$) for the as-deposited $SiO_x$ thin films.

| Sample ID | $E_u$ (meV) | $E_g$ (eV) | Steepness Parameter ($\sigma$) | Constant, $\alpha_0$ ($cm^{-1}$) |
|---|---|---|---|---|
| @1.4 | 523.45 | 3.98 | 0.049 | $10^{4.1}$ |
| @1.6 | 178.48 | 4.18 | 0.145 | $10^{4.8}$ |
| @2.0 | 172.85 | 4.21 | 0.150 | $10^{5.1}$ |

Figure 9 graphically compares the variation of $E_u$ and $E_g$ versus the $O_2$ gas flow rate utilized in the fabrication of the $SiO_x$ thin films.

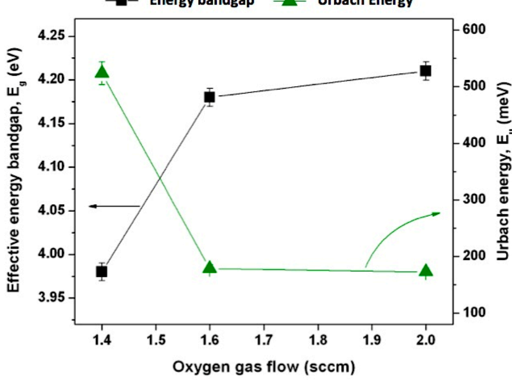


**Figure 9.** Variation of the Urbach energy and bandgap energy as a function of $O_2$ gas flow for the as-deposited $SiO_x$ films.

It can be observed that the Urbach energy comes opposite to the behavior of the energy bandgap. In fact, Figure 9 shows that the $E_u$ value increased with the increase in the Si content (Si-rich $SiO_x$ films). This behavior can be explained and analyzed on the basis of Mott and Davis's model [48,49] for disordered materials. The increase in the deviation from the stoichiometric structure (i.e., the increase of silicon content at the expenses of oxygen) may lead to the increase in the disorder and formation of some defects in the films, which could produce localized states in the material then resulting in the increment of the $E_u$ value in the band structure and, consequently, the decreasing the $E_g$ values for samples with higher Si content.

It is also important to note that for the sample deposited with the higher oxygen gas flow (2.0 sccm), the $E_g$ value is far smaller than the well-established absorption edge in $\alpha$-quartz, the crystalline form of $SiO_2$, which occurs at ≈9 eV [50]. There are different opinions in the literature concerning details of the involved optical transitions. In one of the first calculations, Schulter and Chelikowsky [51] predicted a forbidden indirect lowest energy bandgap. However, in a subsequent computational work by Calabrese et al. [52], it was found that the band edge is direct forbidden (at ≈8.9 eV), followed by a direct allowed transition at ≈10.3 eV. Meanwhile, according to a recent review [47], the direct forbidden absorption edge of amorphous $SiO_2$ (occurring in the $K$ point) in terms of the Urbach model gives $E_g \approx 8.7$ eV. Thus, the non-stoichiometric $SiO_x$ holds a wide bandgap that can be adjusted depending on the oxygen content. Starting at a bandgap of 1.7–1.9 eV for non-crystalline Si, the $E_g$ value could theoretically be raised to ≈8.7 eV for stoichiometric $SiO_2$ (see Figure 10).

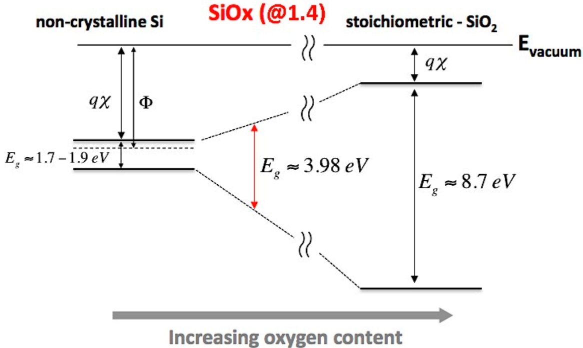


**Figure 10.** Variation of the bandgap energy from 1.7–1.9 eV for a-Si to about 8.7 eV for stoichiometric $SiO_2$, controlled by varying the oxygen concentration (here, $q\chi$ is the electron affinity and $\Phi$ is the electron work function).

For the $SiO_x$ coatings with $x < 2$ the valence band edge moves up, as the increased Si–Si bond states gradually overlap with the oxygen nonbonding states and lastly spread out into the Si valence band [50]. At the same time, the conduction band edge also moves down and, as a net result, a decrease in $E_g$ is observed, as the Si concentration is gradually increased.

Butler and Ginley introduced a theoretical approach to estimate the position of band edges using the following relation [53,54],

$$E_{CB}^{0} = E^{e} - X + \frac{1}{2}E_{g} \tag{6}$$

where

$$X = [x_{\mathrm{Si}}{}^{x} x_{\mathrm{O}}{}^{y}]^{\frac{1}{x+y}} \tag{7}$$

and

$$x_{el} = \frac{1}{2}(A_{el} + I_{el}); el = \mathrm{Si, O} \tag{8}$$

Here $E_{CB}^{0}$ is the conduction band potential, $E^{\mathrm{e}}$ is the energy of free electrons on the normal hydrogen electrode (NHE) scale (4.5 eV), $X$ is the Sanderson electronegativity of the as-deposited material, which is dependent upon the elements of its composition, that is, $X$ is expressed as the geometric mean

of the electronegativities of the constituent atoms. On the other hand, the electronegativities of the constituent atoms are defined as the arithmetic mean of the atomic electron affinity energy, $A_{el}$, and the first ionization energy, $I_{el}$ (both in eV) in which the "*el*" index refers to a particular chemical element. The values of the affinity energies for Si and O elements are 1.39 and 1.46 eV, respectively, while the ionization energies for these elements are 8.15 and 13.62 eV, respectively.

The calculated values of the Sanderson electronegativity, the positions of both the conduction band and the valence band ($E^0_{VB}$) of $SiO_x$ thin films (relative to the NHE scale) are shown in Table 5 and represented in Figure 11.

**Table 5.** The values of the optical energy bandgap ($E_g$), the Sanderson electronegativity ($X$) and the positions of both the conduction and valence bands (relative to the normal hydrogen electrode (NHE) scale) for the produced $SiO_x$ thin films.

| Sample ID | $E_g$ (eV) | $X$ (eV) | $E^0_{CB}$ (eV) (vs. NHE Scale) | $E^0_{VB}$ (eV) (vs. NHE Scale) |
|---|---|---|---|---|
| @1.4 | 3.98 | 6.457 | −0.03 | 3.95 |
| @1.6 | 4.18 | 6.534 | −0.06 | 4.12 |
| @2.0 | 4.21 | 6.539 | −0.07 | 4.15 |

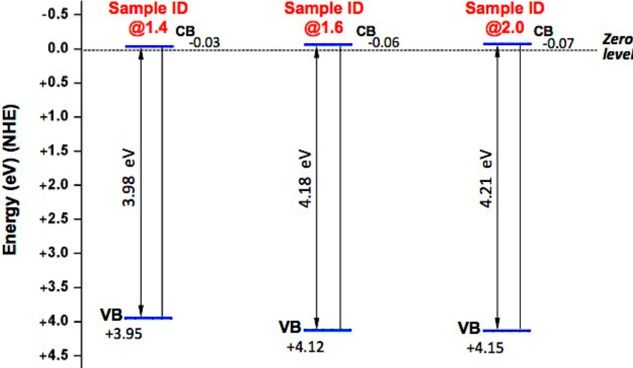


**Figure 11.** The conduction and valence band energy potentials of the $SiO_x$ thin films.

It is observed that the positions of the conduction band and valence band of the as-deposited $SiO_x$ thin films were shifted toward more negative and more positive potentials, respectively by increasing the ratio of the oxygen content of the $SiO_x$ films.

Figure 12 refers to the cross-section SEM micrograph of the sample identified as @1.4. It is noteworthy that in order to carry out SEM analysis, the $SiO_x$ films were firstly deposited on aluminium substrates. This procedure makes easier to visualize and distinguish the different interfaces formed by the as-deposited $SiO_x$ thin film and the Al underlying substrate.

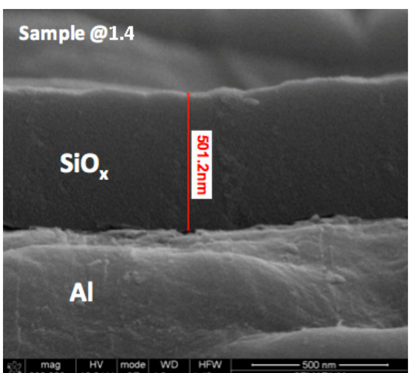


**Figure 12.** Cross-section SEM micrograph referring to the @1.4 $SiO_x$ sample deposited on Al substrate.

From the analysis of SEM micrograph, it can be clearly observed that the as-deposited $SiO_x$ thin film exhibits great compactness (thus, also being an excellent solution in coating' applications for gas diffusion barriers) and presents a high leveling ability, as it exhibits great thickness uniformity along all the surface of the underlying Al substrate.

### 3.3. Current–Voltage Characteristics

Figure 13 shows the *I-V* characteristic of the Au/$SiO_x$/*n*-Si structure (MIS structure) in both linear (Figure 13a) and semi-logarithmic scale (Figure 13b), measured in dark and at room temperature ($T \approx 300$ K, a typical situation in Portugal characterized by high average ambient temperature). The plots in Figure 13, refers to the samples deposited with $O_2$ gas flows of 1.4 and 2.0 sccm and does not include the sample coded as @1.6 because, for this sample, the corresponding characteristic curve practically overlaps with that of sample @2.0, a situation already observed for the case of FTIR measurements and also in optical analysis.

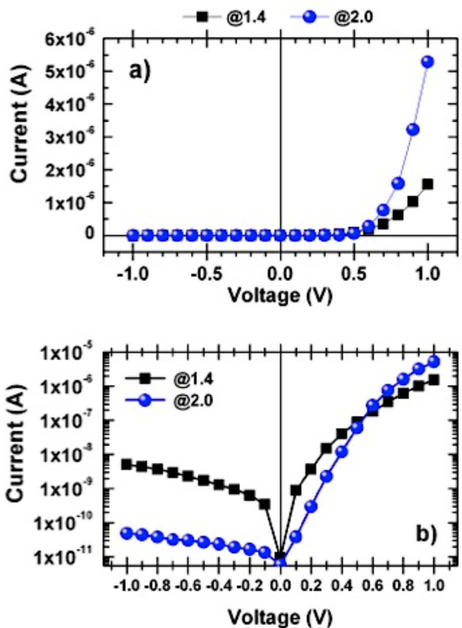


**Figure 13.** Current–voltage characteristic curve of Au/$SiO_x$/*n*-Si structure in dark. Linear (**a**) and semi-logarithmic (**b**) scale.

It is observed that the Au/$SiO_x$/*n*-Si structure (behaving like a Schottky diode) exhibits a very good diode rectifying performance with a rectification ratio of 300 and up to $10^4$, which refer to the @1.4 and @2.0 samples, respectively. These values were calculated by taking the ratio of $I_F/I_R$ at 1 V, where $I_F$ and $I_R$ stands for the forward and reverse current, respectively.

For both samples, the forward current increases exponentially (see Figure 13a) till reaching the series-resistance ($R_S$) limited region, which is characterized by a descending curvature (see Figure 13b). It is well-known that for an ideal diode the standard *I-V* characteristic curve can be expressed by the thermionic emission model [55]

$$I(V) = I_0\left[\exp\left(\frac{qV}{nk_BT}\right) - 1\right] \tag{9}$$

where $V$ is the applied voltage, $n$ is the ideality factor, $q$ is the electron charge and $I_0$ is reverse saturation current due to the minority carriers, which can be given by:

$$I_0 = SA^*T^2\exp\left(\frac{q\varphi_b}{k_BT}\right) \tag{10}$$

where $q\varphi_b$ is the apparent Schottky barrier height for zero-bias point at the interface, $S$ is the area of the rectifier contact and $A^*$ is the effective Richardson constant.

The reverse current, $I_{R,}$ in Figure 13b ($-1 < V < 0$) V, provides valuable information about the device structure. As observed from Figure 13b the *I-V* curves quite differ from the linearity at high reverse bias voltage. The measured current values grow with the increase in reverse applied bias voltage and scale up gradually with the reverse bias without any influence of saturation for all the devices. In this case, non-saturating behavior of reverse current can be explained in terms of the image force lowering of the barrier height due to unstable O and H presence. Moreover, $I_R$ for the @1.4 sample is about two orders of magnitude greater than that for the @2.0 sample at −1 V. The measurements of $I_R$ values have been carried out under dark conditions, at room temperature, which may have been sufficient to promote the generation of thermal carriers, whose contribution for $I_R$ could differ from sample to sample and depends on the energy band characteristics. Noteworthy is that, in general, the higher values of reverse current were registered for sample @1.4, which is the one with the highest Urbach energy and the lowest bandgap value and also oxygen-deficient, thus eventually facilitating the excitation of charge carriers by thermal generation.

The equation that governs an ideal diode makes certain assumptions. Firstly, it assumes a low-level injection of carriers across the junction and also the resistance of the diode in different non-homogenous regions is neglected. However, for a real diode, a number of non-idealities are usually found and this should be taken into consideration to perform its characterization and the ideal diode equation is usually written in the form (9) with $I_0 \rightarrow I_{\text{parts}}$ and $n \rightarrow n_{\text{parts}}$, applied to a limited range of $V$.

Such a relation is the so-called by-parts diode equation and highlights that some particular mechanisms play a dominant role in certain regions of the diode's *I-V* characteristic curve. For most of cases, it is usual to analyze two different regions in the real diode's *I-V* characteristic curve, in which certain mechanisms dominate the current flow. These two regions are the designated by diffusion region (where the dominant current mechanism is a diffusion process) and the Ohmic depletion region, which in turn, plays a dominant role where the forward current flow already takes much higher values [56]. The majority of effects occurring in the Ohmic region (also known as the high injection level regime) arise from changes in the majority carrier concentrations on both sides of the diode's depletion region.

Thus, $I_{\text{parts}}$ and $n_{\text{parts}}$ are characteristic values depending on the dominant mechanism the causing current flow in a real diode. It is important to refer that the ideality factor, $n_{\text{parts}}$ not only takes into account the different current flow mechanisms, but it also depends on unwanted defects eventually introduced at the $SiO_x$/*n*-Si interface during the deposition process. According to Equation (9), the ideality factor of the Au/$SiO_x$/*n*-Si structure was determined from the slope of the straight line taken in the diffusion region of the forward *I-V* characteristic curve plotted in the logarithmic scale, $[qV/(n_{\text{parts}} \times k_B \times T)]$. For the purpose of identifying the two abovementioned regions in an *I-V* characteristic curve of a real diode, Figure 14 shows the *I-V* characteristic for the forward-biased Au/$SiO_x$/*n*-Si real diode referring to the sample identified as @2.0, which refers to the sample deposited with the higher $O_2$ gas flow.

The series diode resistance, $R_S$ was determined by taking the reciprocal of the slope of the tangent to the corresponding *I-V* curve in the higher injection region, that is $R_S = (dI/dV)^{-1}$. Regarding the sample @2.0, the calculated values for the ideality factor and series diode resistance are 2.07 and 65.7 kΩ, respectively. For the sample @1.4 we have the values of $n = 3.03$ and $R_S \approx 217$ kΩ. Taking into account these findings (in particular, the excellent value of the ideality factor for sample @2.0), it is possible to state that the $O_2$ gas flow has a crucial influence on the rectifying performance of the produced Au/$SiO_x$/*n*-Si Schottky diodes since, both $n$ and $R_S$ decrease with the growth of the oxygen content. It possibly reflects a closer approximation to the full stoichiometric condition. The increase of both $n$ and $R_S$ of sample @1.4 may suggest eventual changes in the diffusion mechanism of charge carriers, which may be due to the presence of a greater number of defects and disorder in the $SiO_x$/*n*-Si interface formed during the deposition process as well as some eventual contribution of the *I-V* setup

employed. The high $n$ values can also be the indication of the presence of an interfacial insulator layer patches at Au/$SiO_x$ interface or wide distribution of low Schottky barrier heights and distribution of interface states at the device interface.

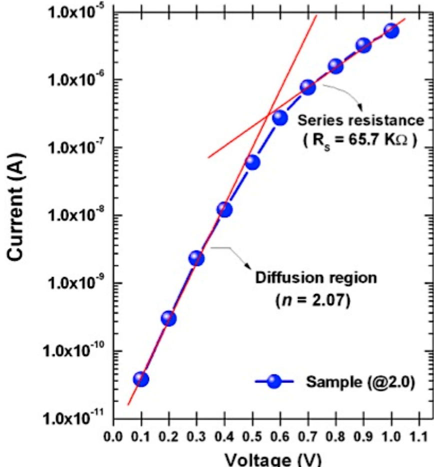


**Figure 14.** *I-V* characteristic curve for the forward-biased Au/$SiO_x$/$n$-Si real diode (@2.0 sample).

## 4. Conclusions

A set of $SiO_x$ thin films were deposited by means of the target voltage control method, a simple procedure of reactive pulsed DC magnetron sputtering (PMS) at three different reactive gas ($O_2$) flow rates. The use of the lowest $O_2$ flow (@1.4) produced Si-rich thin films, while increasing the $O_2$ gas flow facilitated the deposition of oxygen-rich films approaching stoichiometry ($SiO_2$) as proven by IR absorption spectra. The results further suggest that it was the bombardment of the target with $O_2$ gas that promoted a change in the oxidation state of the films being deposited, from silicon excess to a more stoichiometric structure, with Si–O bonds progressively replacing Si–Si bonds. Extending the FTIR spectra to the high-frequency region reveals the presence of $H_2O$ (O–H stretching vibrations) associated with the deposition and attributed to desorbed water from the walls of the vacuum chamber. The presence of $H_2O$ acts as an additional and contaminating source of hydrogen atoms, which possibly compete with the reactive $O_2$ gas to form bonds with the silicon atoms that have been sputtered by $Ar^+$ ion bombardment. In a future project, our deposition chamber will be improved by external application (along the entire diameter of its cylindrical body) of a thermal strap to prevent further contamination with unwanted water vapor.

The dependence of the film's optical characteristics, namely the Urbach energy and energy bandgap, upon the oxygen content was demonstrated, since the lower $O_2$ flow (@1.4) was proven to produce a Si-rich material with a larger Urbach tail and a narrower optical bandgap. It can be associated to the presence of more defects and a greater degree of disorder, which probably arises from an additional contamination source due to the presence of water vapor in the vacuum chamber during the deposition process.

Moreover, it is observed that the Au/$SiO_x$/$n$-Si structure exhibits a Schottky diode rectifying behavior with a rectification ratio of about two orders of magnitude, between @1.4 and @2.0 samples, suggesting the device interface to be relatively free of interface states. Additionally, the above results have confirmed, that the PMS is a useful deposition method for $SiO_2$ and the deposited thin film characteristics depend primarily on the $O_2$ gas flow rate. Therefore, in a future article, the entire range of the $O_2$ flow ratios shown in Figure 2 will be used to cover all the different deposition modes in order to study additional properties related to interlayers and barrier diffusion of $SiO_x$ thin films included under the scope of an on-going project.

**Author Contributions:** Conceptualization, J.O.C., V.T., M.F.C. and A.P.S.; Methodology, J.O.C., M.I.V., L.R., V.T., M.F.C. and A.P.S; Software, F.M.; Validation, J.O.C., M.I.V, V.T., M.F.C., S.L.M, L.R. and A.P.S.; Formal Analysis,

J.O.C., M.I.V., M.F.C. and S.L.M.; Investigation, J.O.C., F.M., M.I.V, M.F.C., S.L.M, L.R. and A.P.S.; Resources, J.O.C., M.I.V, S.L.M, L.R. and V.T.; Data Curation, J.O.C., F.M. and A.P.S.; Writing—Original Draft Preparation, J.O.C.; Writing—Review and Editing, J.O.C., M.I.V, V.T., M.F.C., F.M. and A.P.S.; Visualization, F.M.; Supervision, J.O.C., M.I.V, S.L.M, L.R. and V.T.; Project Administration, J.O.C.; Funding Acquisition, J.O.C., M.I.V, S.L.M, L.R. and V.T.

**Funding:** This work was supported by the Portuguese Foundation for Science and Technology (FCT) in the framework of the Strategic Funding UID/FIS/04650/2019.

**Conflicts of Interest:** The authors declare no conflict of interest.

## References

1. López, J.A.L.; Valerdi, D.E.V.; Lara, A.B.; Salgado, G.G.; Hernández-de la Luz, A.D.; Sánchez, A.M.; Flores Gracia, F.J.; Dominguez, M.A. Optical and compositional properties of $SiO_x$ films deposited by HFCVD: Effect of the hydrogen flow. *J. Electron. Mater.* **2017**, *46*, 2309. [CrossRef]
2. Liao, N.; Xue, W.; Zhou, H.; Zhang, M. Investigation on high temperature fracture properties of amorphous silicon dioxide by large-scale atomistic simulations. *J. Mater. Sci. Mater. Electron.* **2013**, *24*, 1575–1579. [CrossRef]
3. Jiew, C.; Chien, Y.; Yung, R. Development of a robust 2T-SONOS cell for embedded flash application. In Proceedings of the Non-Volatile Memory Technology Symposium (NVMTS, 12), Singapore, 31 October–2 November 2012; pp. 1–6.
4. Leterrier, Y. Durability of nanosized oxygen-barrier coatings on polymers—Internal stresses. *Prog. Mater. Sci.* **2003**, *48*, 1–55. [CrossRef]
5. Dennler, G.; Houdayer, A.; Segui, Y.; Wertheimer, M.R. Growth and structure of hyperthin $SiO_2$ coatings on polymers. *J. Vac. Sci. Technol. A* **2001**, *19*, 2320–2327. [CrossRef]
6. Madou, M.J. *Fundamentals of Microfabrication: The Science of Miniaturization*, 2nd ed.; CRC Press LCC: Boca Raton, FL, USA, 2002.
7. Nicollian, E.H.; Brews, J.R. *MOS (Metal Oxide Semiconductor) Physics and Technology*; Wiley: New York, NY, USA, 1982.
8. Nakano, Y.; Jimbo, T. Electrical characterization of $SiO_2$/n-GaN metal–insulator–semiconductor diodes. *J. Vac. Sci. Technol. B Microelectron. Nanometer Struct.* **2003**, *21*, 1364–1368. [CrossRef]
9. Fedder, G.K. Mems fabrication. In Proceedings of the 2003 International Test Conference (ITC 2003): Breaking Test Interface Bottlenecks, Charlotte, NC, USA, 28 September–3 October 2003; Volume 1, pp. 691–698.
10. Wright, J.T.; Carbaugh, D.J.; Haggerty, M.; Richard, A.L.; Ingram, D.C.; Jadwisienczak, W.M.; Rahman, F.; Kaya, S. Thermal oxidation of silicon in a residual oxygen atmosphere—The RESOX process—For self-limiting growth of thin silicon dioxide films. *Semicond. Sci. Technol.* **2016**, *31*, 105007. [CrossRef]
11. Adams, A.C.; Smith, T.E.; Chang, C.C. The growth and characterization of very thin silicon dioxide films. *J. Electrochem. Soc.* **1980**, *127*, 1787–1794. [CrossRef]
12. Boyd, I.W.; Wilson, J.I. A study of thin silicon dioxide films using infrared absorption techniques. *J. Appl. Phys.* **1982**, *53*, 4166–4172. [CrossRef]
13. Jun, S.I.; McKnight, T.E.; Melechko, A.V.; Simpson, M.L.; Rack, P.D. Characterisation of reactively sputtered silicon oxide for thin-film transistor fabrication. *Electron. Lett.* **2005**, *41*, 822–823. [CrossRef]
14. Carneiro, J.; Teixeira, V.; Martins, A.; Mendes, M.; Ribeiro, M.; Vieira, A.; Carneiro, J. Surface properties of doped and undoped $TiO_2$ thin films deposited by magnetron sputtering. *Vacuum* **2009**, *83*, 1303–1306. [CrossRef]
15. Sainty, W.G.; Netterfield, R.P.; Martin, P.J. Protective dielectric coatings produced by ion-assisted deposition. *Appl. Opt.* **1984**, *23*, 1116–1119. [CrossRef] [PubMed]
16. Alvisi, M.; De Tomasi, F.; Della Patria, A.; Di Giulio, M.; Masetti, E.; Perrone, M.R.; Protopapa, M.L.; Tepore, A. Ion assistance effects on electron beam deposited $MgF_2$ films. *J. Vac. Sci. Technol. A* **2002**, *20*, 714–720. [CrossRef]
17. Jaing, C.-C.; Shiao, M.-H.; Lee, C.-C.; Lu, C.-J.; Liu, M.-C.; Lee, C.-H.; Chen, H.-C. Effects of ion assistance and substrate temperature on optical characteristics and microstructure of $MgF_2$ films formed by electron-beam evaporation. *Jpn. J. Appl. Phys.* **2006**, *45*, 5027–5029. [CrossRef]
18. Megiris, C.E.; Glezer, J.H.E. Preparation of silicon dioxide films by low-pressure chemical vapor deposition on dense and porous alumina substrates. *Chem. Eng. Sci.* **1992**, *47*, 3925–3934. [CrossRef]

19. Hayashi, S.; Tanimoto, S.; Yamamoto, K. Analysis of surface oxides of gas-evaporated Si small particles with infrared spectroscopy, high-resolution electron microscopy, and x-ray photoemission spectroscopy. *J. Appl. Phys.* **1990**, *68*, 5300–5308. [CrossRef]
20. Teixeira, V.; Soares, P.; Martins, A.J.; Carneiro, J.; Cerqueira, F.; Cerqueira, M.F. Nanocomposite metal amorphous-carbon thin films deposited by hybrid PVD and PECVD technique. *J. Nanosci. Nanotechnol.* **2009**, *9*, 4061–4066. [CrossRef] [PubMed]
21. Sellers, J. Asymmetric bipolar pulsed DC: The enabling technology for reactive PVD. *Surf. Coat. Technol.* **1998**, *98*, 1245–1250. [CrossRef]
22. Kelly, P.; Beevers, C.; Henderson, P.; Arnell, R.; Bradley, J.; Bäcker, H. A comparison of the properties of titanium-based films produced by pulsed and continuous DC magnetron sputtering. *Surf. Coat. Technol.* **2003**, *174*, 795–800. [CrossRef]
23. Studenyak, I.; Kranjčec, M.; Kurik, M. Urbach rule in solid state physics. *Int. J. Opt. Appl.* **2014**, *4*, 76–83.
24. Schottky, W. Zur Halbleitertheorie der Sperrschicht- und Spitzengleichrichter. *Z. Phys.* **1939**, *113*, 367–414. [CrossRef]
25. Tung, R.T. The physics and chemistry of the Schottky barrier height. *Appl. Phys. Rev.* **2014**, *1*, 011304.
26. Zhang, Z.; Yates, J.T., Jr. Band bending in semiconductors: Chemical and physical consequences at surfaces and interfaces. *Chem. Rev.* **2012**, *112*, 5520–5551. [CrossRef] [PubMed]
27. Carneiro, J.; Teixeira, V.; Portinha, A.; Magalhães, A.; Coutinho, P.; Tavares, C.J.; Newton, R.; Carneiro, J.; Magalhaẽs, A. Iron-doped photocatalytic $TiO_2$ sputtered coatings on plastics for self-cleaning applications. *Mater. Sci. Eng. B* **2007**, *138*, 144–150. [CrossRef]
28. Carneiro, J.O.; Teixeira, V.; Nascimento, J.H.O.; Neves, J.; Tavares, P.B.; Carneiro, J. Photocatalytic activity and UV-protection of $TiO_2$ nanocoatings on poly(lactic acid) fibres deposited by pulsed magnetron sputtering. *J. Nanosci. Nanotechnol.* **2011**, *11*, 8979–8985. [CrossRef] [PubMed]
29. Barradas, N.; Jeynes, C.; Webb, R.; Kreissig, U.; Grötzschel, R. Unambiguous automatic evaluation of multiple ion beam analysis data with simulated annealing. *Nucl. Instrum. Methods Phys. Res. Sect. B Beam Interact. Mater. At.* **1999**, *149*, 233–237. [CrossRef]
30. Musil, J.; Baroch, P.; Vlček, J.; Nam, K.; Han, J. Reactive magnetron sputtering of thin films: Present status and trends. *Thin Solid Film.* **2005**, *475*, 208–218. [CrossRef]
31. Ohring, M. *The Materials Science of Thin Films*; Academic Press: San Diego, CA, USA, 1991.
32. Sigmund, P. Theory of sputtering. I. Sputtering yield of amorphous and polycrystalline targets. *Phys. Rev.* **1969**, *184*, 383. [CrossRef]
33. Kudriavtsev, Y.; Villegas, A.; Godines, A.; Asomoza, R. Calculation of the surface binding energy for ion sputtered particles. *Appl. Surf. Sci.* **2005**, *239*, 273–278. [CrossRef]
34. Ay, F.; Aydinly, A. Comparative investigation of hydrogen bonding in silicon based PECVD grown dielectrics for optical waveguides. *Opt. Mater.* **2004**, *26*, 33–46. [CrossRef]
35. Lin, G.-R.; Lin, C.-J.; Lin, C.-K.; Chou, L.-J.; Chueh, Y.-L. Oxygen defect and Si nanocrystal dependent white-light and near-infrared electroluminescence of Si-implanted and plasma-enhanced chemical-vapor deposition-grown Si-rich $SiO_2$. *J. Appl. Phys.* **2005**, *97*, 094306. [CrossRef]
36. Pai, P.G.; Chao, S.S.; Takagi, Y.; Lucovsky, G. Infrared spectroscopic study of silicon oxide ($SiO_x$) films produced by plasma enhanced chemical vapor deposition. *J. Vac. Sci. Technol. A* **1986**, *4*, 689–694. [CrossRef]
37. Vázquez-Valerdi, D.E.; Luna-López, J.A.; Carrillo-López, J.; García-Salgado, G.; Benítez-Lara, A.; Espinosa-Torres, N.D. Compositional and optical properties of $SiO_x$ films and ($SiO_x$/$SiO_y$) junctions deposited by HFCVD. *Nanoscale Res. Lett.* **2014**, *9*, 422. [CrossRef] [PubMed]
38. Morioka, T.; Tsuda, N.; Koike, C.; Kaito, C.; Saito, Y.; Kimura, S. Study of the structure of silica film by infrared spectroscopy and electron diffraction analyses. *Mon. Not. R. Astron. Soc.* **1998**, *299*, 78–82. [CrossRef]
39. Ogata, Y.; Niki, H.; Sakka, T.; Iwasaki, M. Oxidation of porous silicon under water vapor environment. *J. Electrochem. Soc.* **1995**, *142*, 1595–1601. [CrossRef]
40. Gupta, P.; Dillon, A.; Bracker, A.; George, S. FTIR studies of $H_2O$ and $D_2O$ decomposition on porous silicon surfaces. *Surf. Sci.* **1991**, *245*, 360–372. [CrossRef]
41. Hassanien, A.S.; Akl, A.A. Influence of composition on optical and dispersion parameters of thermally evaporated non-crystalline $Cd_{50}S_{50-x}Se_x$ thin films. *J. Alloys Compd.* **2015**, *648*, 280–290. [CrossRef]
42. Tauc, J.; Grigorovici, R.; Vancu, A. Optical Properties and electronic structure of amorphous germanium. *Phys. Status Solidi* **1966**, *15*, 627–637. [CrossRef]

43. Urbach, F. The long-wavelength edge of photographic sensitivity and of the electronic absorption of solids. *Phys. Rev.* **1953**, *92*, 1324. [CrossRef]
44. Malainho, E.; Vasilevskiy, M.I.; Alpuim, P.; Filonovich, S.A. Dielectric function of hydrogenated amorphous silicon near the optical absorption edge. *J. Appl. Phys.* **2009**, *106*, 073110. [CrossRef]
45. Hassanien, A.S.; Akl, A.A. Effect of Se addition on optical and electrical properties of chalcogenide CdSSe thin films. *Superlattices Microstruct.* **2016**, *89*, 153–169. [CrossRef]
46. Kazmersky, L.L. (Ed.) *Polycrystalline and Amorphous Thin Films and Devices*; Academic Press: New York, NY, USA, 1980; p. 135.
47. Nekrashevich, S.S.; Gritsenko, V.A. Electronic structure of silicon dioxide (a review). *Phys. Solid State* **2014**, *56*, 207–222. [CrossRef]
48. Mott, N.F.; Davis, E.A. *Electronic Processes in Non-Crystalline Materials*; Oxford University Press: Oxford, UK, 1971.
49. Fadel, M.; Fayek, S.; Abou-Helal, M.; Ibrahim, M.; Shakra, A. Structural and optical properties of SeGe and $SeGe_X$ ($X$ = In, Sb and Bi) amorphous films. *J. Alloys Compd.* **2009**, *485*, 604–609. [CrossRef]
50. Choi, Y.-R.; Zheng, M.; Bai, F.; Liu, J.; Tok, E.-S.; Huang, Z.; Sow, C.-H. Laser-induced greenish-blue photoluminescence of mesoporous silicon nanowires. *Sci. Rep.* **2014**, *4*, 4940. [CrossRef] [PubMed]
51. Schlüter, M.; Chelikowsky, J. Electron states in α-quartz ($SiO_2$). *Solid State Commun.* **1977**, *21*, 381–384. [CrossRef]
52. Calabrese, E.; Fowler, W.B. Electronic energy-band structure of α quartz. *Phys. Rev. B* **1978**, *18*, 2888–2896. [CrossRef]
53. Butler, M.A. Prediction of flatband potentials at semiconductor-electrolyte interfaces from atomic electronegativities. *J. Electrochem. Soc.* **1978**, *125*, 228–232. [CrossRef]
54. Morrison, S.R. *Electrochemistry at Semiconductor and Oxidized Metal Electrodes*; Plenum Press: New York, NY, USA, 1980.
55. Chen, X.Y.; Lu, Y.F.; Tang, L.J.; Wu, Y.H.; Cho, B.J.; Xu, X.J.; Dong, J.R.; Song, W.D. Annealing and oxidation of silicon oxide films prepared by plasma-enhanced chemical vapor deposition. *J. Appl. Phys.* **2005**, *97*, 014913. [CrossRef]
56. Bo, H.; Ma, Z.Q.; Jing, X.; Lei, Z.; Sheng, Z.N.; Feng, L.; Cheng, S.; Ling, S.; Jie, M.X.; Yue, Z.C.; et al. Structural, electrical and optical properties of AZO/$SiO_2$/p-Si SIS heterojunction prepared by magnetron sputtering. *Opt. Appl.* **2010**, *40*, 15–24.

© 2019 by the authors. Licensee MDPI, Basel, Switzerland. This article is an open access article distributed under the terms and conditions of the Creative Commons Attribution (CC BY) license (http://creativecommons.org/licenses/by/4.0/).